Evidence of hot high velocity photoionized plasma falling on actively accreting T-Tauri Stars.

Ana Ines Gómez de Castro	
Grupo de Investigación Complutense AEGORA an	nd S.D. Astronomía y Geodesia, Fac. de
CC Matemáticas, Universidad Complutense, 28040 Madrid, Spain	
Received; acce	epted

ABSTRACT

The HeII(1640Å) line and the resonance doublet of NV(UV1) provide a good diagnostic tool to constrain the excitation mechanism of hot ($T_e > 40,000$ K) atmospheric/magnetospheric plasmas in T Tauri Stars. Making use of the data available in the Hubble Space Telescope Archive, this work shows that there are, at least, two distinct physical components contributing to the radiation in these tracers: the accretion flow sliding on the magnetosphere and the atmosphere.

The NV profiles are symmetric and at rest with respect to the star, in most sources. The velocity dispersion of the profile increases from non-accreting ($\sigma = 40 \text{ km s}^{-1}$) to accreting ($\sigma = 120 \text{ km s}^{-1}$) TTSs suggesting that the macroturbulence field in the line formation region decreases as the stars approach the main sequence. Evidence of the NV line being formed in a hot solar-like wind has been found in RW Aur, HN Tau and AA Tau.

The HeII profile has a strong narrow component that dominates the line flux; the dispersion of this component ranges from 20 to 60 km s⁻¹. The source of this radiation is uncertain. Current data suggest that both accretion shocks and atmospheric emission might contribute to the line flux. In some sources, the He II line shows a broad and redwards shifted emission component often accompanied by semiforbidden O III] emission that has a critical electron density of $\sim 3.4 \times 10^{10}$ cm³.

In spite of the different origins (inferred from the kinematics of the line formation region), NV and HeII fluxes are strongly correlated, with the only possible exception of some of the heaviest accretors.

Subject headings: stars: pre-main sequence, stars: magnetic fields

1. Introduction

Solar-like pre-main sequence (PMS) stars and, in general, the low mass PMS stars $(M_* < 2M_{\odot})$, or T Tauri stars (TTSs), are complex dynamical systems made of two basic components, star and accretion disk, as well as a dynamical interface, the stellar magnetosphere (see Gómez de Castro 2013, for a recent review). Magnetic fields of few kG have been detected in the surface of the TTSs (Guenther et al 1999; Johns-Krull et al 1999; Johns-Krull et al 1999; Johns-Krull et al 2007). The surface field is not bipolar but it has a rather complex structure as the Sun's field has (Johns-Krull et al 2004). Hence, though higher order, multi-polar components fall off more rapidly with radius than the dipolar field, it is difficult to track the final path followed by matter from the inner disk border to the stellar surface. In addition, the magnetosphere has its own dynamics and forcing due to the interaction with the disk.

Unfortunately, the characteristics of the TTSs extended atmosphere and magnetospheres are still escaping the diagnosis (see Hartmann 2009). Little is known about them, apart from having a density of $\sim 10^9-10^{11}$ cm⁻³ and an electron temperature between some few thousand Kelvin and 100,000 K (Gómez de Castro & Verdugo 2007, hereafter GdCV2007). Recent attempts to derive the magnetospheric properties from optical lines have shown that, for instance, the H α profile is strongly dependent on densities and temperatures assumed inside the magnetosphere and in the disk wind reagion (Lima et al. 2010). The line widths of typical atmospheric/magnetospheric tracers are about 200-300 km/s that exceed by far what expected from thermal or rotational broadening even if the lines are assumed to be formed in a magnetosphere that extends to some 4-5 stellar radii and corotates with the star. As today, it is still unclear whether the broadening is produced by unresolved macroscopic flows or by magnetic waves propagating on the magnetospheric field (Hartmann et al. 1982). In general, the broadening of magnetospheric tracers does not vary significantly in time, pointing out that the average motions are rather stable. The

combined effect of funnel flows and inclined magnetic rotators as simulated by Romanova et al (2004,2012) is the current baseline for the numerical simulation of TTSs magnetospheres. The stellar field is assumed to be anchored in the inner part of the disk creating a sheared layer between the rigid body rotation of the star and the Keplerian rotation of the disk. This interaction has a profound influence on the star and the accretion flow but also acts as a dynamo that transform part of the angular momentum excess in the inner disk into magnetic field amplification that self-regulates through quiescent periods of field building-up and eruptions when the energy excess is released (see Gómez de Castro & von Rekowsky 2011, for an evaluation of the UV output from such interface). However, magnetospheric heating processes are poorly known and accretion shock models are unable to predict the observed line fluxes/broadening (Johns-Krull 2009).

The atmospheric and magnetospheric energy output is released mainly in the ultraviolet. The richness of spectral tracers for a broad range of magnetospheric temperatures and densities is unmatched by any other range. There are several studies of the atmospheric/magnetospheric properties of the TTSs based on low dispersion UV data (Lemmens et al. 1992, Huélamo et al. 1998, Johns-Krull et al. 2000, Yang et al. 2012, Gómez de Castro & Marcos-Arenal, 2012, hereafter GdCMA2012). However, only the Cosmic Origins Spectrograph (COS) (see Green et al 2012 for a description of the instrument), on board the Hubble Space Telescope (HST), has been sensitive enough to gather high signal-to-noise ratio (SNR) profiles of hot plasma tracers such as the N V [UV1] resonance multiplet or the He II H α transition with a resolution above 10,000 in late K and M-type TTSs (see Penston & Lago 1984 for C IV profiles obtained with the IUE, Ardila et al 2002, for HST profiles obtained with the Goddard High Resolution Spectrograph and Ayres 2005, for the CoolCat set based on HST data obtained with the Space Telescope Imaging Spectrograph and compare them with the presented in Sect. 2).

Following a previous work where the magnetospheric properties of TTSs were examined based on low dispersion HST data (GdCMA2012), the high resolution profiles of the N V [UV1], O III] and He II(1640 Å) transitions are analysed in this work with two main objectives. Firstly, it is intended to determine whether it is feasible to discriminate the contribution to the high energy radiation flux from the high density atmospheric plasma and from the accretion flow. Moreover, the unexpected correlation between X-ray flux and the high energy UV tracers found by GdCMA2012 is re-examined on the light of the kinematic information contained in the high resolution HST/COS profiles. In Sect. 2 the observations are described. The results are presented in Sect. 3. Two components are found to contribute to the He II flux a Low Density Component (LDC) associated with the accretion flow and a High Density Component (HDC) of more uncertain origin. The discussion on the possible source of the HDC, its association with accretion shocks and the properties of the LDC are addressed in Sect. 4. The article concludes with a brief summary on the relevance of these results.

2. Hubble Space Telescope (HST) observations

The He II profiles of TTSs in the Taurus-Aurigae star forming region have been retrieved from the HST archive. Only high resolution observations have been considered. Most of them have been obtained with the Cosmic Origins Spectrograph (COS) and the gratings G130M and G160M. The resolution is ~24,000 and each target has been observed three times with slight offsets in the wavelength range to guarantee that the 18.1Å gap between the two segments in the FUV detector is covered (see COS Handbook). Moreover, some few TTSs have been observed with the Space Telescope Imaging Spectrograph (STIS), namely, T Tau, DR Tau, and DF Tau. Only the T Tau profile had a high enough signal-to-noise ratio (SNR) in the He II line to be considered for this work. The log of

the observations is provided in Table 1; additional information on the HST programs that obtained these observations (programs IDs. 11533, 11616 and 8627) can also be found in the Table.

The observational strategy allowed to search for variations in the profiles in time scales of ~ 20 minutes but neither flux, nor morphology were found to display significant changes. The one-dimensional spectra produced by the COS calibration pipeline (CALCOS v2.17.3) were aligned and co-added¹. COS targets must be centred to within 0.1 - 0.2 arcsec to achieve the nominal wavelength accuracy of $\pm 15 \text{ km s}^{-1}$. The (R(3) 1-7) 1489.636 Å and (P(5) 1-7) 1504.845 Å H₂ lines have been used to set the zero of the wavelength scale for the targets in Table 1. H₂ emission is dominated by the molecular disk around the stars in most sources (France et al. 2012). The lines have been selected to be strong (from Herczeg et al. 2002) and detectable in most of the sources. The profiles of the 1489.636 A line are plotted in Figure 1 (see also Figure 3 in France et al. 2012) and the He II profiles are plotted in Figure 2. No shifts have been applied to DN Tau and IP Tau observations because the H₂ emission was too weak to be used for this purpose. Neither shifts have been applied to HBC 427, LkCa 19 and LkCa 4 because H₂ emission was not detected. The H₂ profiles are sometimes asymmetric with respect to the rest wavelength, very especially in RW Aur. In this case, the original zero from the CALCOS pipeline has been left. Only a subset of AA Tau observations has been used since guide star acquisition failed (see Fig. 3). As a result, the first two exposures produced similar profiles while the last one produces a slightly broader and more red-shifted (by $\sim 0.1 \rm \AA~or~18~km~s^{-1}$ at 1640 Å) profile. For this star, the last observation was rejected and only the two first observations were averaged to

¹Note that there are small wavelength windows in the spectra without flux measurements. This effect has been taken into account in the calculation of the average spectra from the, typically, three observations obtained per star.

produce the profiles in Figs. 1 and 2.

The He II profiles can be generically described as composed of a bright and narrow emission feature and a broad, weaker component that differs from one star to another. Notice that the He II lines are very strong; this fact, together with the strong H₂ emission, contributes to the continuum jump in the low resolution Advanced Camera System on HST reported by GdCMA2012.

Close to the He II line, there are the O III]₁₆₆₅ intercombination lines; a doublet with components at $\lambda\lambda 1660.802$ and 1666.156, which originate under transitions from the level $2s2p^3$ 5S_2 to the term $2s^22p^2$ 3P with J=1 and J=2, respectively. The components should have an intensity ratio $\simeq 1:3$; equal to the ratio of their transition probabilities (145 s⁻¹ and 426 s⁻¹). The transition is optically thin to a critical density of 3.4×10^{10} cm⁻³. The O III] profiles are represented in Fig. 4. The two lines of the multiplet are observed in GM Aur, DF Tau, HN Tau, DR Tau, SU Aur, RW Aur and DE Tau; however the flux of the weakest, 1660.802 Å line, has only been measured for strong sources. In all cases, the flux ratio between the two lines of the multiplet is 1:3 (within the error bars).

To complete the view on the distribution of hot plasma in the TTSs environment, also the profiles of the resonance UV 1 multiplet of the N V have been retrieved from the HST archive (see Table 2). In the blue edge of the 1238.8 Å line, the strongest in the doublet, there are some narrow emission lines produced by molecular hydrogen (lines: $\lambda 1237.918$ Å 1-2 P(8), $\lambda 1237.589$ Å 2-2 R(11)) that somewhat blur the profile. The zero of the wavelength scale has been set again, resourcing to H₂ emission lines. The (P(2) 0-4) 1338.63 Å line has been used for this purpose, since it is strong in most of the stars and it is not blended with other features (see Figure 5 with the H₂ profiles). As mentioned above, the original zero of the wavelength scale has not been shifted for DN Tau, IP Tau, HBC 427, LkCa 19 and LkCa 4 because the H₂ lines were either very weak or absent. The N V profiles can be

most generally described by a single component that ranges from being narrow in stars like HBC 427, LkCa 19 and LkCa 4 to be broad and asymmetric in AA Tau or GM Aur (see Fig. 6).

Some relevant properties of the TTSs to be used in Sect. 3 are gathered in Table 3. Notice that there are wide variations in published values of important parameters such as the stellar luminosity or the extinction (see also comments in GdCMA2012); data in Table 3 are gathered for reference for other researchers. The X-ray fluxes have been retrieved from the XMM-Newton extended survey of the Taurus molecular cloud (XEST) (Guedel et al. 2007). The He II, the 1238.82 Å N V and the O III] lines fluxes have been measured after subtracting the local continuum. Also the fluxes for the 1489.636 and 1338.63 H₂ lines have measured (see Sect. 5). The lines fluxes are provided in Table 4; they are not extinction corrected. For some sources, the measurement of the 1238.82 Å N V flux has required subtracting the nearby H₂ features. In such cases, the H₂ flux has been subtracted by linear interpolation in the N V profile. However, there are some few profiles where this linear interpolation was uncertain (see quality flags in Table 4).

3. Results

From figures 1 to 6 a generic trend can be inferred:

- The weak-line TTSs (WTTSs) in the sample, i.e. evolved TTSs with no evidence of mass infall (LkCa 19, LkCa 4, HBC 427), do not display H₂ emission, neither nebular O III] emission. They have only rather narrow He II and N V lines.
- Intermediate objects (TTSs) like IP Tau, DN Tau and V836 Tau have weak H₂ and no nebular O III] emission. Both He II and N V lines have narrow emission profiles.
- The Classical TTSs (CTTSs) emit in all these tracers (see below).

CTTSs cover a broad range of profiles morphologies. Strong H₂ emission is detected in all of them and the lines are narrow unless in RW Aur A (see France et al 2012). Nebular O III] emission is detected in all of them unless in DM Tau, UX Tau A and AA Tau. O III] is especially strong in T Tau, DF Tau, HN Tau, DR Tau and RW Aur. SU Aur, and DE Tau seem to be intermediate objects. Hints of possible O III] emission at 1666 Å are seen in GM Aur, unfortunately the S/N is low and the weakest component of the multiplet is not detected. A low S/N feature is detected at 1666 AA in DN Tau, IP Tau, AA Tau and UX Tau spectra. Observations of the C III] intercombination transition line are only available for three of the stars in the sample, namely, DE Tau, T Tau and RW Aur and no significant differences have been found between the O III] and the C III] profiles obtained either with the Goddard High Resolution Spectrograph (GHRS) (compare Fig. 4 with Fig.1 in Gómez de Castro et al 2001) and STIS (compare Fig. 4 with Fig.1 in Gómez de Castro et al 2003).

In general, the He II profiles can be described by a narrow emission component superimposed on a broader contribution that mimics the observed in the O III] nebular lines, when high enough S/N data profiles are observed. This effect is clearly apparent in HN Tau and RW Aur. Note that in DR Tau and DF Tau, the overlap is lost at bluewards shifted velocities; there is bluewards shifted O III] emission with no He II counterpart. This bluewards shifted excess could be caused by the contribution of an unresolved jet to the line emission. As shown for RY Tau by GdCV2003, the semiforbidden emission has two components: one associated with the jet and another with the accretion flow that were disentangled for this source due to their variability. The N V profiles however, do not follow the same morphological trend. A rather narrow symmetric profile is observed in DE Tau that becomes wider in DM Tau, DF Tau, UX Tau A, GM Aur and SU Aur, all of them sources with absent or weak O III] nebular emission. DR Tau, HN Tau, RW Aur and AA Tau display very peculiar profiles that clearly indicate that N V emission is not

produced in the stellar atmosphere but in another dynamical component. In particular, the N V profiles of RW Aur, HN Tau and AA Tau are asymmetric extending from red-wards shifted velocities to peak at blue-wards shifted velocities; moreover, the RW Aur profile peaks at the velocity of the optical jet (Hirth et al 1997) that was also detected in the C III] intercombination line by Gómez de Castro & Verdugo, 2003. This type of profile asymmetry has also been detected in the C III] profile of RY Tau (GdCV2007), who pointed out that the line could be formed in a pre-main sequence analogue of the Solar wind. In this context, it is worth remarking that the H₂ profile of RW Aur has a completely different asymmetry, the flux peaks to the red of the line, suggesting the presence of infalling cold molecular gas similar to that observed in the pre-main sequence close binary AK Sco (see also Gómez de Castro et al 2013).

These groups can be cleanly recognised in velocity dispersion diagrams. The characterisation of the underlying velocity field and thermal properties of the line emission region is complex in the TTSs environment. Instead of using the standard fitting to Gaussian or Voight profiles, it is preferable to characterise the profile in terms of the standard Pearson statistics moments and measures, i.e., mean or centroid, dispersion, kurtosis and skewness. They provide a quantitative measurement of the deviation of the profile from the expected for a thermal plasmas; a normal distribution convolved with the Line Spread Function (LSF) of COS (Kriss 2011). Note that in this approach, the profile is assumed to be formed by the contribution to the line flux of independent gas parcels, i.e. the (background subtracted) profile is treated as a histogram of the flux emitted per parcel in the wavelength (velocity) space; a similar approach was followed by GdCV2007 to compare the observed C III] and Si III] profiles of RY Tau with the theoretical predictions. This treatment permits to characterise the profiles that are formed in complex velocity fields. In Table 5, the dispersions of the He II and N V lines are provided together with that obtained for two control lines, the H₂ transitions at 1339Å and 1489Å; RW Aur,

HN Tau and AA Tau are not included because their N V profiles are peculiar. As shown in the bottom panel of Fig. 8, the average dispersion of the H_2 profiles is 31 ± 5 km s⁻¹ and $43 \pm 13 \text{ km s}^{-1}$ for the 1339Å and 1489Å lines, respectively. There is not any correlation between the broadening of these two H₂ lines, pointing out that the scattering of the dispersions in the diagram is related with random effects associated with the measurement process. A different trend is drawn from the N V and He II dispersions. The dispersions of the WTTSs and DN Tau are comparable to those measured in the H_2 line. In intermediate objects, like V836Tau and IP Tau, the dispersions in the He II line are comparable to those measured in the H₂ lines but the N V lines are significantly broader. Finally in the CTTSs both $\sigma(N V)$ and $\sigma(He II)$ are larger than $\sigma(H_2)$. Note that stellar rotation may contribute to the line dispersion; SU Aur, the fastest rotator in the sample has also the largest dispersion. However, a large dispersion can also be produced by the profile asymmetry. For instance, DM Tau has dispersions comparable to those measured in SU Aur and it is one of the slowest rotators in the sample (see Table 3). Two objects do not follow this trend: DR Tau and DE Tau, both have intermediate dispersions in the N V lines and large dispersions in the He II lines caused by the broad emission component. A quick inspection in the summary of the TTSs properties (see Table 3) indicates that the only possible cause of this discrepancy is the high accretion rate, as otherwise, expected.

3.1. Two hot plasma components in the TTSs

From figures 2, 4 and 6, it is clearly inferred that there are, at least, two different plasmas contributing to the spectral lines under study:

• A low density component (LDC) that it is most conspicuously traced by the O III] line. The LDC also produces the He II broad emission component observed in RW Aur, HN Tau, DR Tau and DF Tau. The critical density of the O III] sets an

upper limit to the electron density² of the plasma in the LDC of $\simeq 3.4 \times 10^{10} {\rm cm}^{-3}$, (see also Sect. 4.2). The LDC profiles display a non-thermal broadening and draw a complex velocity field around the stars, i.e., it is not associated to a simple standing atmospheric structure whose kinematics is dominated by stellar rotation. In fact, the LDC profiles seem to rather trace some kind of complex magnetospheric infalling pattern, high above the stellar surface. Also, in some cases, could be associated to unresolved wind structures (Gómez de Castro & Ferro-Fontán 2005), as the reported for RY Tau (GdCV2007). Notice that the co-existence of O III] and He II radiation from the same kinematic structure would point out an unrealistically high electron temperatures for the line emission region (log $T_e(K) \sim 5.4$), if collisional equilibrium at a single temperature is assumed and electron densities below the O III] critical density are considered³. In fact, its UV spectrum is reminiscent of that observed in photoionized nebulae (see also Sect. 4). To the current sensitivity, the contribution of this component to the N V flux is negligible.

A high density/temperature component (HDC) that dominates the N V emission.
O III] profiles are very different from N V profiles suggesting that the density is of the
N V formation region is higher than the O III] critical density.

Though the kinematics of the N V emission region is clearly different from that traced by the LDC, the N V flux is correlated with the He II flux as shown in Fig. 9; the Spearman rank correlation coefficient is $r_s = 0.87$ (with significance level, $\alpha = 0.001$, see Sachs 1982 for details) and,

² Note that for electron densities above the critical density, there may still be line emission though it damps rapidly.

³Calculations made using the Chianti data base: www.chiantidatabase.org.

$$\log (F(HeII)) = (0.8 \pm 0.1) \log (F(NV)) - (2.5 \pm 1.7)$$

with RMS = 0.29 (see bottom panel in Fig. 9). Also the fluxes normalised to the stellar surface are correlated with $r_s = 0.82$, with $\alpha = 0.002$ (see top panel in Fig. 9) and,

$$\log \left(\frac{F(L(HeII))}{F_{\text{bol}}} \right) = (0.9 \pm 0.1) \log \left(\frac{F(NV)}{F_{\text{bol}}} \right) + (0.0 \pm 0.6)$$

with an RMS=0.31. The normalised flux is defined as the rate $F_{HeII}/F_{bol,*}$ or $F_{NV}/F_{bol,*}$ and was introduced by GdCMA2021 to provide a measure of the line emissivity weighted over an unknown thickness but corrected from stellar radii and surface temperature. In this manner, the normalised fluxes compensate for scaling effects associated with the broad range of mass, luminosity and stellar radius covered by the TTSs. Stars whose He II flux has a significant contribution from the LDC are marked in the plot. Notice that they are evenly distributed in the figure suggesting that He II and N V fluxes are correlated, independently of whether the He II flux is dominated by the narrow emission component.

3.2. The connection between UV and the X-ray radiation from the TTSs

Based on low resolution observations, GdCMA2012 pointed out that the normalised He II flux anti correlates with the strength of the X-ray flux as derived in the XEST survey (Guedel et al 2007) carried out with the XMM-Newton telescope in the 0.3-10.0 keV band. In Fig. 10, the normalised He II fluxes from the high resolution COS/HST observation (see Table 3) are represented against the normalised X-ray luminosities as derived from the XEST survey. Also the Chandra/ACIS observations of LkCa 4, DE Tau, GM Aur from Yang et al. (2012) are used; they are integrated X-ray luminosities in the 0.3-10 keV range. The He II flux has been extinction corrected according to Valencic et al (2004) assuming R=3.1 and extinctions in Table 3. The low dispersion, GdCMA2012 data, have been

also plotted for those sources with no available high dispersion data. There is significant contribution to the He II flux from the LDC in some few sources: SU Aur, HN Tau, DE Tau and DM Tau, that are marked in the figure. A first inspection of the Fig 10, shows three groups. The WTTSs (HBC 427, LkCa 4, HD283472), UX Tau and the fast rotator SU Aur are very close to the main sequence stars regression line. The CTTSs follow the generic trend pointed out by GdCMA2012, the He II flux increases as the X-ray flux decreases. Notice that the sources with strong LDCs are far from this trend, excluding the fast rotator SU Aur. If HN Tau, DE Tau and DM Tau are excluded, the Spearman rank correlation coefficient is $r_s = -0.591$, with $\alpha = 0.033$, and the least square fit is,

$$\log\left(\frac{F(L_X)}{F_{\text{bol}}}\right) = (-0.20 \pm 0.05)\log\left(\frac{F(HeII)}{F_{\text{bol}}}\right) - (4.3 \pm 0.2)$$

with RMS = 0.15. Uncertainties in the A_V values may produce a shift towards large f_{HeII} in the plot reinforcing the trend; note that the regression line runs nearly parallel to the extinction direction. To examine its effect, the same diagram has been plotted in the bottom panel of Fig 10 using, stellar luminosities, X-ray luminosities and A_V values from the recent compilation by Yang et al (2012). As shown, the three groups are no so cleanly separated and the regression line is more clear; only DE Tau is far from the trend and has been excluded from the calculation. The results are similar though the negative slope is softer:

$$\log\left(\frac{F(L_X)}{F_{\text{bol}}}\right) = (-0.17 \pm 0.07)\log\left(\frac{F(HeII)}{F_{\text{bol}}}\right) - (4.1 \pm 0.1)$$

with RMS = 0.15 and $r_s = -0.561$, with $\alpha = 0.036$.

In summary, though the clean separation between WTTSs and accreting TTSs may be an extinction associated effect, the trend to release preferentially the high energy excess in the UV rather than in the X-ray channel in accreting objects holds with the only possible exception of the sources with a strong contribution the He II flux from the LDC.

From the current data sets and observations, it cannot be ascertain whether there is a

statistically meaningful deviation of the sources with strong LDCs from the main trend. Unfortunately, there are not X-ray measurements of DR Tau or DF Tau and RW Aur was only detected to have a low soft X-ray flux with the EINSTEIN satellite (Damiani et al 1995). If present, such a trend could indicate that X-ray radiation is dominated by different components in sources with strong LDCs (strong nebular component) and in sources with weak or absent LDCs. The X-rays energy distribution of the TTSs is often modelled by two components: a soft component at $T_s \simeq (2-5)~10^6~\mathrm{K}$ and a hard component at $T_h \simeq (1.5-3)~10^7~{\rm K}$ (see i.e. Glassgold et al, 2000). The hard X-ray component is thought to be associated with magnetic energy release in the stellar coronae. The nature of the soft X-ray component is more uncertain and often, it has been hypothesised that could be formed in accretion shocks (Lamzin 1998, Gullbring et al 1998). Unfortunately, only three stars in our sample namely, T Tau, SU Aur and HBC 427 have a high enough count rate to allow a spectral fitting to two different optically thin plasmas and non-conclusive results could be derived from the fits (see Table 6 with the two-components fit to the X-ray spectrum of these sources (from Table 6 in Guedel et al. (2007)). The X-ray spectrum of SU Aur, a CTTS, is dominated by the low temperature component with T=5.22 MK however, both soft and hard X-ray component, have similar emission measures in HBC 427,a non-accreting WTTSs. Moreover, the hard X-ray component dominates the X-ray spectrum of the CTTS, T Tau.

4. Discussion

TTSs are complex objects; they are convective PMS stars where a solar-like dynamo begins to set in, while still the fossil magnetic field is diffusing. TTSs are surrounded by an external dynamo that powers and makes rise the stellar magnetosphere to the inner border of the molecular disk (see Romanova et al 2012 for recent simulations). Matter from the

disk, slides down onto the star along the magnetospheric field lines to end, free-falling onto the open holes of the magnetic configuration. In this environment, hot plasma radiating in the UV tracers studied in this work can be located in the magnetosphere, in the atmosphere, in the accretion shocks and also in the outflow (either solar-like or driven from the star-disk magnetic interface or the disk). Both, magnetosphere and outflow, have significantly lower densities than the stellar atmosphere or the accretion shocks; as a result, spectral lines radiation is dominated by radiative de-excitation processes and forbidden and semiforbidden transitions are strong from this plasma. In the dense atmosphere, collisional de-excitation is relevant and forbidden transitions are quenched. UV semiforbidden transitions cannot be observed from the accretion shock itself, because it is too hot and dense however, the soft X-ray radiation produced in the shock front photoionizes the preshock gas, which has a density similar to that of the stellar magnetosphere and may produce forbidden lines radiation (Gómez de Castro & Lamzin, 1999). Unfortunately, the high column density prevents the UV radiation from the photoionization cascade to escape easily from the accretion column. Also, the profiles of some tracers, from the infrared He I transition (Beristain et al. 2001, Fisher et al. 2008) to the UV lines do not agree with the predictions of accretion shock models (Johns-Krull 2009). Within this context, the data presented in Sect. 3 provide some amazing results:

- The He II, O III] and N V fluxes do not depend on the spectral type. This confirms that the line emission is not dominated by main sequence like atmospheric magnetic activity, i.e. with the release of the magnetic energy produced by the stellar dynamo, since this one depends on the spectral type (see e.g. Ayres et al 1995 and GdCM2012).
- The He II and N V fluxes correlate well independently of whether the line profiles are very different, e.g., independently of whether the line emission is produced in the same physical structure. This confirms that all processes (accretion, atmospheric emission

and outflow) are coupled, as otherwise expected (see Gomez de Castro 2013 for a recent review). In turn, it makes difficult to get specific tracers of individual processes without the kinematical information, *i.e.* without high resolution spectroscopy.

- The high resolution profiles of the N V line show a symmetric line broadening that increases from non accreting to accreting stars, being significantly suprathermal in these last sources (see Table 5). The profile shape and the density of the line formation region suggests an atmospheric origin (with the exceptions already mentioned in Sect. 3). The connection between line broadening and accretion suggests that the density and extent of the high atmospheric layers depends on the accretion rate, i.e. on the evolutionary state, as otherwise predicted from the theoretical models (D'Antona & Mazzitelli 1997, Siess et al 2000). Transport of magnetic energy from the stellar interior to the surface is expected to occur at a different pace in accreting sources than in WTTSs. Moreover, the extended magnetosphere powered by the disk-star magnetic locking, must affect the stellar atmosphere introducing new sources of stirring and turbulence (see e.g. Kivelson & Russell, 1995).
- However, the physical source of the narrow emission component in the He II profile keeps being uncertain. It could either be associated with accretion shocks or with atmospheric features.

In this section, the possible source of the He II narrow emission component is analysed as well as some constraints on the extent of the magnetosphere inferred from the semiforbidden line radiation.

4.1. On the source of the narrow component of the He II line: accretion shocks or bulk atmospheric phenomena?

The kinematics of the region where the narrow component forms, is clearly distinct from that of the N V or the O III] lines formation region (see Fig. 8). The dispersion of the narrow emission component of the He II ranges from $\sim 20 \text{ km s}^{-1}$ to $\sim 60 \text{ km s}^{-1}$ while the dispersion of the N V line varies varies from $\sim 40 \text{ km s}^{-1}$ to $\sim 130 \text{ km s}^{-1}$ for the same sources (see Fig. 11). The dispersion of the narrow emission component in the He II profile has been evaluated as above (see Sect.3) but setting an upper wavelength cut-off to reject the contribution of the LDC. Note that even setting this cut-off there is an unknown contribution from the LDC to the flux.

Moreover, the narrow component seems to be slightly redshifted in *all* sources, from 24 km s^{-1} in UX Tau to 37 km s^{-1} in DE Tau (see Appendix 1 and Table 7). Hence, it would be tempting to suggest that the line is produced in accretion shocks.

Accretion shocks are produced by the impact of the free-falling material from the disk onto the stellar surface. The kinetic energy of the infalling matter, with typical free-fall speeds of $\sim 300~\rm km~s^{-1}$ is involved into gas heating at the shock front that reaches temperatures of about 1MK. The soft X-ray radiation from the shock front is expected to photoionize (pre-ionize) the infalling gas column (see i.e. Lamzin 1998, Gómez de Castro & Lamzin 1999, Muzerolle et al 2001, Orlando et al 2009). Also, the shock front could back illuminate the stellar surface, becoming a source of atmospheric photoionization to be added to the coronal X-ray radiation. In this context, the narrow component of the He II line could be produced very close to the shock front. The slight, but small redshift, could be interpreted as an indication of the line being formed in postshock material, and the small width could be caused by thermal broadening; the thermal velocity of fully ionized, solar abundance plasma at 50,000 K is 23 km s⁻¹. However, this cannot be concluded

from these data alone. Firstly, the apparent redshift could be caused by the blending of the narrow component with the broad component which is asymmetric in most sources, $e.\ g.$, with very low or absent flux at bluewards shifted velocities. The line broadening is affected by the same problem though no so dramatically given the relative strengths of the narrow and broad components. Unfortunately, unless very high S/N profiles (~ 100) of the semiforbidden and the He II lines are obtained, any fitting is hampered by these uncertainties. Finally, it is also, intriguing that the broadening of the He II emission line in non-accreting TTSs, such as LkCa 4, LkCa 19 and HBC 427, is comparable to the observed in UX Tau or in V836 Tau that are TTSs with low accretion rates. In this respect, it is worth noticing that the correlation between the He II flux and the accretion luminosity, as derived from the U-band excess (Ingleby et al 2009, Gullbring et al 1998) is mild⁴, as shown in Fig. 12 (see also GdCMA2012).

Taking into account all these facts, as well as the good correlation between the He II and the N V fluxes (Fig. 9) and the convergence of the He II and N V lines broadenings towards the non-accreting WTTSs, a contribution to the narrow component of the He II line from the stellar atmosphere cannot be neglected. In summary, the data analysed in this work are non-conclusive concerning the source of the narrow component of the He II line. For all the reasons mentioned above, it is most probable that both physical components, accretion shocks and stellar atmosphere, contribute to the flux.

⁴Note that the He II flux and the accretion luminosity measurements are not simultaneous. However, the variability of the HeII flux and, in general, of the UV tracers (continuum lines) is typically smaller than a factor of 2 (Gómez de Castro & Franqueira 1997; Huélamo et al. 2000). Measurements of the accretion rate are based in the U-band excess that also varies typically by this amount (Gullbring et al 1998).

4.2. Properties of the LDC

The profiles produced in the LDC cannot be ascribed to a simple kinematics shared by all sources, neither the radiating plasma can be modelled by simple collisional plasma models. However, some constraints on its overall physical properties can be derived from the ratios of the intercombination lines of O III], Si III] and C III]. The plasma density can be constrained from the Si III]/C III] ratio (Gómez de Castro & Verdugo 2001). The detection of O III]_{1661,1666} can be used to fix up the temperature since the O III]/Si III] ratio is very sensitive to it.

The Si III] and C III] lines have been observed with STIS for three sources in the sample: RW Aur (Gómez de Castro & Verdugo 2003, hereafter GdCV2003), DE Tau and T Tau (Gómez de Castro et al 2003). T Tau profiles display a non-negligible contribution from the large scale jet. DE Tau Si III] and C III] profiles are rather narrow and similar to the O III] line. From RW Aur study, GdCV2003 pointed out that the emitting volume is clumpy with a rather small filling factor, as otherwise expected if magnetospheric radiation is produced in plasma filaments and clumps. This clumpy nature together with the broad temperature range covered by the various spectral tracers suggest that the excitation mechanism could be photoionization instead of collisional excitation.

GdCV2003 produced two grids of photonionization models to explore possible regimes for line excitation making use of CLOUDY (Ferland 1996), a code designed to simulate emission line regions in astrophysical environments. The first set assumed that LDC had a belt like geometry, being illuminated by the ambient X-ray radiation field: soft and hard components, at 3.5×10^6 K and 2.8×10^7 K respectively, with a total X-rays luminosity of 3×10^{29} erg s⁻¹. This model turned out to be unable to reproduce comparable strengths of the three spectral tracers. However, if the O III], Si III] and C III] emission is assumed to be produced in dense gas around small X-ray sources, such as reconnecting loops, the lines

ratios could be reproduced for electron densities of $n_e \geq 10^{11}$ cm⁻³. For soft X-ray sources, with $T_e = 10^6$ K, luminosities of 10^{27} erg s⁻¹ and radii of 10^8 cm⁻³, the inferred O III] emissivity is $\sim 10^{-3.5}$ erg s cm⁻². Using this one as a fiducial value, an estimate of the LDC volume, V_{LDC} could be derived from the line strength as, $\frac{V_{LDC}}{\eta} = \frac{F(OIII)^{4\pi d^2}}{\epsilon_{OIII}}$ where F(OIII]) is the reddening corrected line flux and η is the filling factor of the hot plasma. For filling factors of 10, and assuming that the emission is concentrated in a spherical shell of radius R_{LDC} and thickness $0.01R_{LDC}$, LDC radii from 4 to 9 R_{\odot} are inferred. These values are within a factor of 1.5 of the magnetospheric radii derived from accretion luminosities for stars with known magnetic fields (Johns-Krull 2007, GdCMA2012). Unfortunately, the uncertainties in the plasma distribution prevent more detailed evaluations.

5. Conclusions

The UV radiation from N V, He II and O III] is dominated by the contribution of three main components of the TTSs atmospheric/magnetospheric environment: the magnetospheric flow of infalling matter, the disturbed upper atmospheric layers and the accretion shock.

The diffuse magnetospheric plasma (LDC) is best traced by the O III] line: it produces asymmetric profiles, preferentially red-shifted. He II emission is observed from the same kinematical structures that radiate in O III]. This plasma is not excited by thermal collisions at a single electron temperature. In fact, there are indications that photoionization processes could be significant.

The hot, dense layers of the stellar atmosphere are best traced by the N V line. However, the line dispersion increases steadily with the accretion rate suggesting a connection between the disturbances in the upper atmospheric layers and the accretion flow.

The He II flux is dominated by a narrow emission component of uncertain origin. In this work, we have presented evidences indicating that it may be formed in hot postshock material in accretion shocks but also, evidences of its connection with atmospheric tracers. Both accretion shocks and the upper atmospheric layers seem to contribute to the narrow component of the He II profile.

The anticorrelation between X-ray and UV flux found but GdCMA2012 has been confirmed, suggesting that the dissipation of magnetic energy proceeds in the TTSs differently than in main sequence stars. The denser environment produced by mass accretion (see i.e. Petrov et al. 2011) seems to favour the ultraviolet channel for the dissipation of the magnetic energy excess.

All the observations indicate that the UV radiation field during PMS evolution is much harder than the usually implemented in the modelling of protostellar disks evolution. An example of its effect in the dust grains charging and charging profile can be found in Pedersen & Gómez de Castro 2011. Theoretical modelling of protostellar disks chemistry and life generation environments should take this fact into account.

Kevin France brought to my attention the HST/COS data corresponding to AA Tau. The analysis of the data pointed out that the 1640Å jump in the HST/ACS data was dominated by an unexpectedly strong He II line. This article has grown from extending this analysis to the TTSs observed with HST/COS. I would like to thank an anonymous referee for suggesting the use of the $\rm H_2$ lines to set the zero of the wavelength scale. This work has been partly funded by the Ministerio de Economia y Competitividad of Spain through grant AYA2011-29754-C03-C01.

A. The velocity of the He II narrow emission component

The narrow emission component of the He II line seems to be systematically red-shifted with respect to the H_2 lines. The shifts are small ($\sim 0.16 \text{ Å or } 29 \text{ km s}^{-1}$) as shown in Table 8. The zero of the wavelength scale has been set with the (R(3) 1-7) 1489.636 Å and $(P(5) 1-7) 1504.845 \text{ Å H}_2$ lines because they were observed in most of the stars. These lines are far from the 1640 Å He II line and, in principle, small uncertainties in the wavelength calibration could drive to these shifts. However, as shown in Figures 14 and 15, this is not the case. The P(17)3-9 line is plotted for the whole sample in Figure 14 though only is clearly observed in: DM Tau, UX Tau A, AA Tau, GM Aur and DR Tau (the H₂ emission from RW Aur cannot be used for this purpose). In all cases, the ${\rm H}_2$ transition is at rest. In Figure 15, the C I[uv1] multiplet is plotted. It is observed as narrow emission lines in DN Tau, DM Tau, UX Tau A and DF Tau. In all cases, the lines are at rest wavelength. This red-shift is observed both in CTTSs and intermediate objects (it cannot be measured in WTTSs because of the lack of H_2 emission). Thus, unless the P(14) 3-10 H_2 transition, that it is blended with the He II line, is unusually strong, it must be concluded that the narrow emission component of the HeII line is red-shifted in most sources. Note however, that the blending with the broad component could produce an apparent redshift if this broad component is asymmetric.

Facilities: HST (COS), HST (STIS), XMM-Newton (EPIC).

REFERENCES

- Ardila, D. R., Basri, G., Walter, F. M., et al. 2002, ApJ, 566, 1100
- Ayres, T. R., Fleming, T. A., Simon, T., et al., 1995, ApJS, 96, 223
- Ayres, T.R., 2005, Proceedings of the 13th Cambridge Workshop on Cool Stars, Stellar Systems and the Sun, held 5-9 July, 2004 in Hamburg, Germany. Edited by F. Favata, G.A.J. Hussain, and B. Battrick. ESA SP-560, European Space Agency, p.419
- Beristain, G., Edwards, S., Kwan, J., 2001, ApJ, 551, 1037
- Bertout, C., Siess, L. and Cabrit, S., 2007, Astronomy & Astrophysics, 473, L21–L24
- Brown, A. de M. Ferraz, M. C. and Jordan, C., 1984, Royal Astronomical Society, 207, 831
- Clarke, C.J., Bouvier, J., 2000, M.N.R.A.S., 319, 457
- D'Antona, F., & Mazzitelli, I. 1997, Mem. Soc. Astron. Italiana, 68, 807
- Damiani, F., Micela, G., Sciortino, S. et al. 1995, ApJ, 446 331
- Ferland, G., J., 1996, *Hazy, a Brief Introduction to Cloudy*, University of Kentucky, Department of Physics and Astronomy Internal Report.
- Fischer, W., Kwan, J., Edwards, S. et al., 2008, ApJ, 687, 1117
- France, K., Schindhelm, E., Herczeg, G. J. et al. 2012, ApJ, 756, 171
- Glassgold, A. E., Feigelson, E. D., Montmerle, T., 2000, Protostars and Planets IV (Book Tucson: University of Arizona Press; eds Mannings, V., Boss, A.P., Russell, S. S.), p. 429
- Gómez de Castro, A.I. & Lamzin, S., 1999, Monthly Notices of the R.A.S., 304, L41

Gómez de Castro, A. I., & Verdugo, E. 2001, ApJ, 548, 976

Gómez de Castro, A. I., & Verdugo, E. 2003, ApJ, 597, 443

Gómez de Castro, A.I., Verdugo, E., Ferro-Fontán, C., 2003, The Future of Cool-Star Astrophysics: 12th Cambridge Workshop on Cool Stars, Stellar Systems, and the Sun (2001 July 30 - August 3), eds. A. Brown, G.M. Harper, and T.R. Ayres, (University of Colorado), p. 40-49.

Gómez de Castro, A.I., Ferro-Fontán, C., 2005, MNRAS, 362, 569

Gómez de Castro, A. I., & Verdugo, E. 2007, ApJ, 654, L91

Gómez de Castro, A. I. 2009, ApJ, 698, L108

Gómez de Castro, A.I., von Rekowsky, B., 2011, MNRAS, 411, 849

Gómez de Castro, A.I., Marcos-Arenal, P., 2012, ApJ, 749, 190

Gómez de Castro, A.I. 2013, Planets, Stars and Stellar Systems, Editor-in-chief: Oswalt, T. D. McLean, I.S.; Bond, H.E.; French, L.; Kalas, P.; Barstow, M.A.; Gilmore, G.F.; Keel, W.C. (Eds.), Springer, ISBN 978-90-481-8817-8

Green, J. C., Froning, C. S., Osterman, S. et al. 2012, ApJ, 744, 60

Güdel, M., Briggs, K. R., Arzner, K., et al. 2007, A&A, 468, 353

Guenther E.W., Lehman H., Emerson J.P. et al., A&A, 341, 768, 1999

Hartmann, L., 2009, Protostellar Jets in Context, by Kanaris Tsinganos, Tom Ray, Matthias Stute. Astrophysics and Space Science Proceedings Series. Berlin: Springer, pp.23-32

Hartmann, L., Avrett, E. Edwards, S., 1982, ApJ, 261, 279

Herczeg, G. J., Linsky, J. L., Valenti, J. A., 2002, ApJ, 572, 310

Hirth, G.A., Mundt, R., Solf, J., 1997, Astronomy & Astrophysics Sup., 126, 437

Huélamo, N., Gómez de Castro, A.I., Franqueira, M., 1998, Ultraviolet Astrophysics Beyond the IUE Final Archive, ESA Publications Division, ESA SP, 413, 121

Ingleby, L. Calvet, N., Bergin, E. et al., 2009, ApJ, 703, L137

Johns-Krull, C. M., Valenti, J. A., Koresko, C., 1999, ApJ, 516, 900

Johns-Krull, C. M., Valenti, J. A., & Linsky, J. L. 2000, ApJ, 539, 815

Johns-Krull, C. M., Valenti, J. A., & Saar, S. H. 2004, ApJ, 617, 1204

Johns-Krull, C. M., 2007, ApJ, 664 975

Johns-Krull, C.M., Protostellar Jets in Context, Astrophysics and Space Science Proceedings Series, 33, 2009

Kenyon, S. J. and Hartmann, L., 1995, Ap&SS, 101, 117

Kivelson, M.G., Russel, C.T., 1995, Introduction to space physics, Cambridge Univ. Press, p. 330

Kriss, G.A. 2011, Improved Medium Resolution Line Spread Functions for COS FUV Spectra, Technical Report

Lamzin, S., 1998, Astronomy Reports, 42, 322

Lemmens, A. F. P., Rutten, R. G. M., Zwaan, C. 1992, A&A, 257, 671

Lima, G.H.R.A., Alencar, S.H.P., Calvet, N. et al., 2010, A&A, 522, 104L

Linsky, J. L., Bornmann, P. L., Carpenter, K. G. et al. 1982, ApJ, 260, 670

Muzerolle, J., Calvet, N., Hartmann, L., 1998, ApJ, 492, 743

Muzerolle, J., Calvet, N., Hartmann, L., 2001, ApJ, 550, 994

Neuhauser, R., Sterzik, M.F., Schmidt, J.H.M.M. et al 1995, A&A, 297, 391

Orlando, S., Sacco, G. G., Argiroffi, C. et al., 2009, A&A, 510, 71

Pedersen, A., Gómez de Castro, A.I., 2011, ApJ, 740, 77

Penston, M. & Lago, M.T.V.T., 1983, Monthly Notices of the R.A.S., 202, 77

Petrov, P.P., Gahm, G., F., Stempels, H.C. et al., 2011, A&A, 535, 6

Romanova, M. M., Ustyugova, G. V., Koldoba, A. V. et al., 2004, ApJ, 610, 920

Romanova M. M., Ustyugova, G. V., Koldoba, A. V. et al. 2012, Monthly Notices of the R.A.S., 421, 63

Sachs, L., 1982, Applied Statistics, a handbook of techniques, Springer Series in Statistics, Springer-Verlag, NY (ISBN:0-387-90976-1)

Siess, L., Dufour, E., & Forestini, M. 2000, A&A, 358, 593

Valencic, L. A., Clayton, G. C., & Gordon, K. D. 2004, ApJ, 616, 912

Yang, H., Herczeg, G. J., Linsky, J. L., et al, 2012, ApJ, 744, 121

This manuscript was prepared with the AAS LATEX macros v5.2.

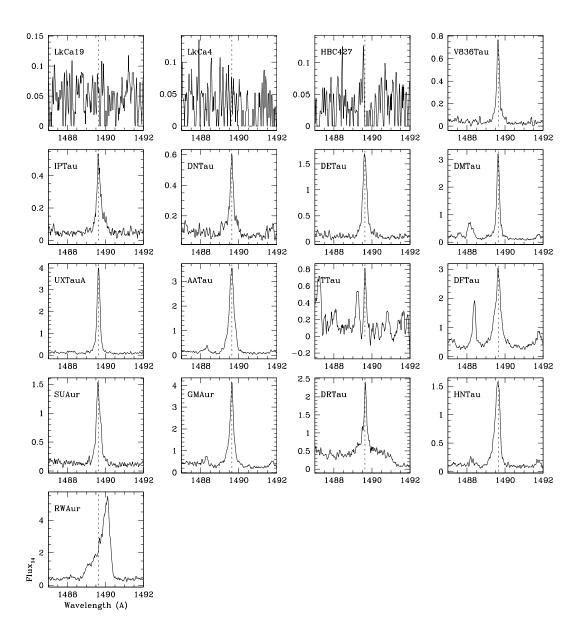


Fig. 1.— Profiles of the (R(3) 1-7) 1489.636 Å H_2 line of the TTSs studied in this work. The zero of the wavelength scale has been set using H_2 lines as reference (see text). Notice the asymmetry and broadening of RW Aur profile that prevents its use for this purpose. Fluxes are given in units of 10^{-14} erg s⁻¹ cm⁻² Å⁻¹ (F₁₄)

.

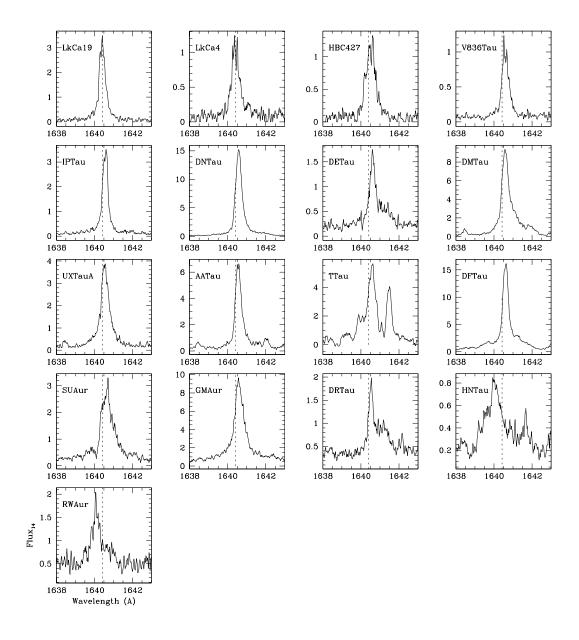


Fig. 2.— He II profiles of the TTSs in Taurus observed with HST. The rest wavelength of the He II line is marked for reference (see also Figure 1). Fluxes are given in units of $10^{-14} \text{ erg s}^{-1} \text{ cm}^{-2} \text{ Å}^{-1} \text{ (F}_{14})$.

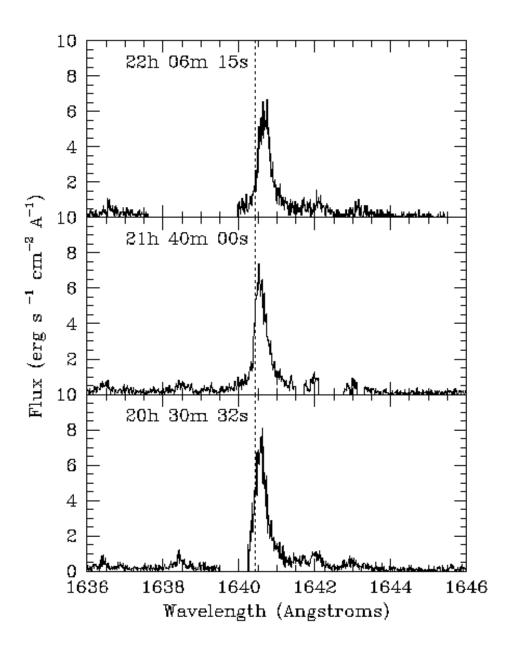


Fig. 3.— The three observations of the He II line in AA Tau with HST/COS. The rest wavelength of the He II line is marked for reference. During the observations the guide star acquisition failed. Note the broadening and shift of the central peak from the first to the last observation.

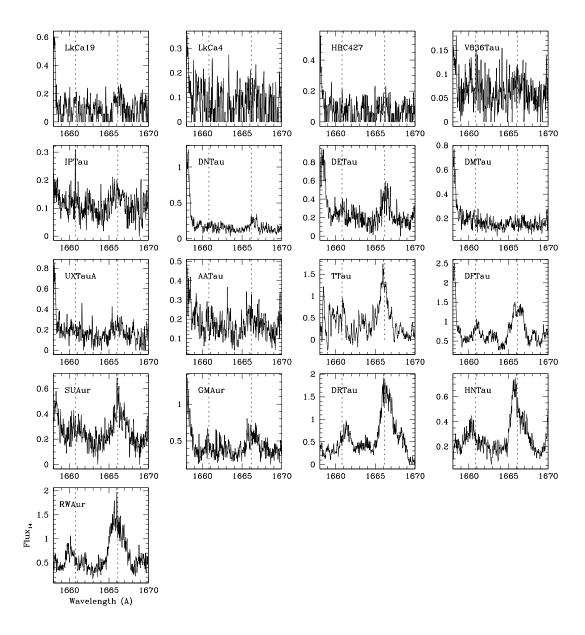


Fig. 4.— O III] profiles of the TTSs in Taurus observed with HST. The rest wavelength of the two lines in the multiplet is marked for reference (see also Table 1). Fluxes are given in units of 10^{-14} erg s⁻¹ cm⁻² Å⁻¹ (F₁₄).

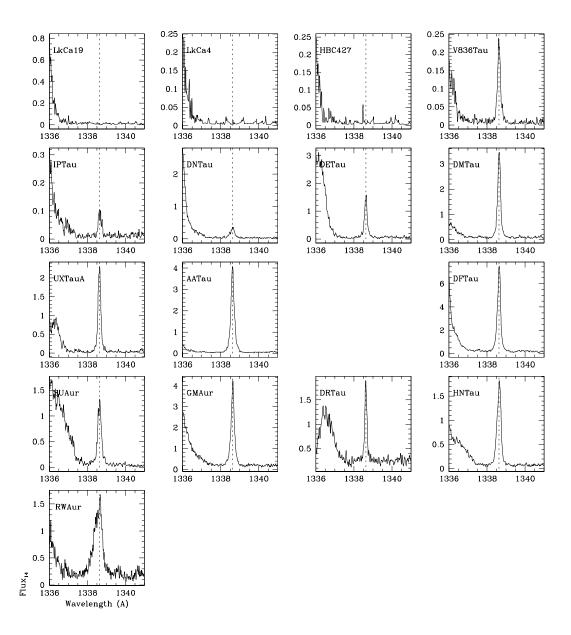


Fig. 5.— Profiles of the (P(2) 0-4) 1338.63 Å H_2 line of the TTSs studied in this work. The zero of the wavelength scale has been set using H_2 lines as reference (see text). Notice the asymmetry and broadening of the RW Aur profile that prevents its use for this purpose. Fluxes are given in units of 10^{-14} erg s⁻¹ cm⁻² Å⁻¹ (F₁₄).

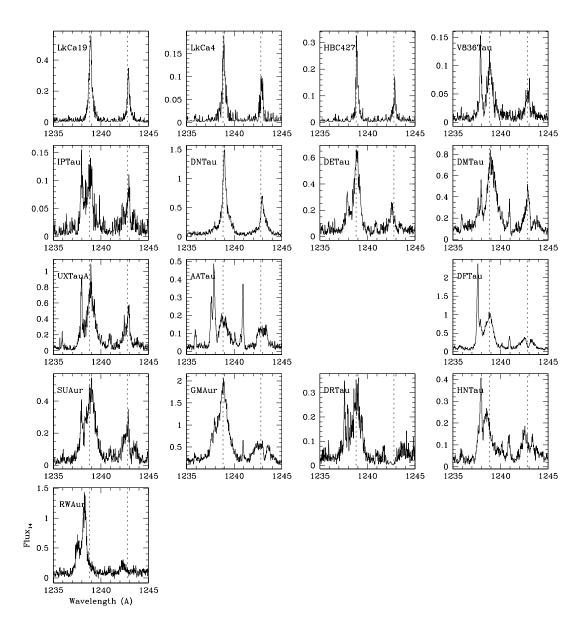


Fig. 6.— N V profiles of the TTSs in Taurus. The rest wavelengths of the N V lines are marked for reference (see also Figure 5). Fluxes are given in units of 10^{-14} erg s⁻¹ cm⁻² Å⁻¹ (F₁₄).

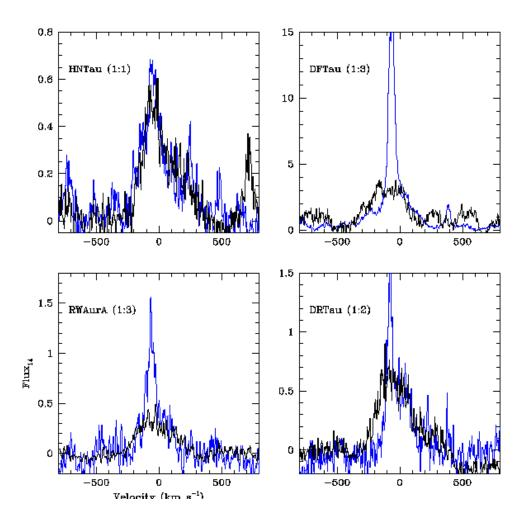


Fig. 7.— High SNR O III] profiles (black) over-plotted on the respective He II profiles (blue). The O III] profiles have been re-scaled for comparison. The scaling factor is indicated in the figure for every profile.

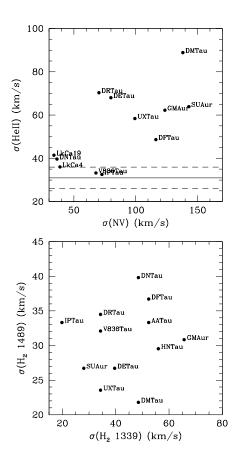


Fig. 8.— Top panel: Broadening of the N V line (dispersion) compared with the broadening of the He II line. The broadening is defined as the dispersion of the profile (see text). For comparison the broadening of the H₂ 1489 Å and 1389 Å lines are plotted in the bottom panel. The dispersion of the N V line is larger than the measured in the H₂ 1389 Å line in all sources. However the dispersion of H₂ 1489 Å is comparable to the observed in the He II line in WTTSs and transitional objects. The average $\sigma(H_2(1489)) = 31\pm 5 \text{ km s}^{-1}$ is represented in the top panel; the solid line represents the average and the error band is marked with dashed lines. Circled sources have a significant contribution from the LDC to the He II flux.

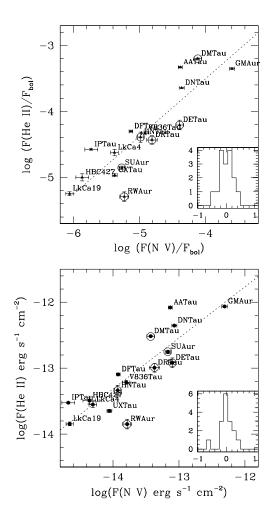
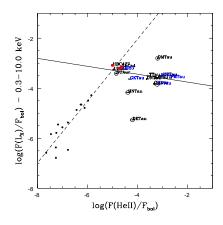


Fig. 9.— *Bottom*: the He II flux is plotted versus the N V flux. *Top*: the He II normalised flux is plotted against the N V normalised flux. Fluxes are extinction corrected. The small insets at the bottom-right corner are the histograms representing the distance of the sources to the main regression line, plotted as a dashed line. Circled sources have a significant contribution from the LDC to the He II flux.



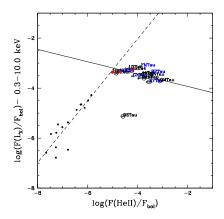


Fig. 10.— Normalised X-ray flux versus normalised He II flux for TTSs compared with main sequence stars cool stars (MSCSs). TTSs are plotted with triangles and the error bars are marked. MSCSs are plotted with filled circles (data from Ayres et al 1995 and Linsky et al 1982, as described in GdCMA2012). The MSCSs regression line is plotted with a dashed line and the TTSs regression line with a continuous line. The stars names are indicated in black for F(He II) measurements based on high resolution data (this work) and in blue for GdCMA2012 measurements based on low dispersion data. Red dots mark WTTSs location. $Top: A_V$, f_{bol} and L_X as in Table 3. Circled sources have a significant contribution from the LDC to the He II flux. $Bottom: A_V$, f_{bol} and L_X as in Table 2 of Hao Yang et al. 2012.

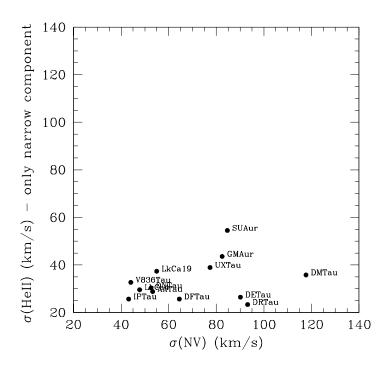


Fig. 11.— As Fig. 8 but the dispersion of the He II line is evaluated only for the narrow component of the profile.

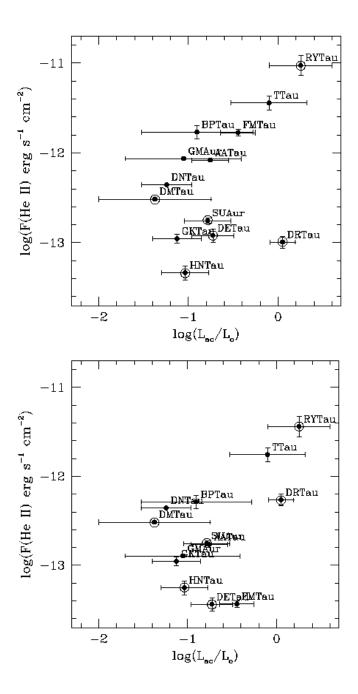


Fig. 12.— Top panel: He II fluxes versus accretion luminosities using extinctions from Table 3. Bottom panel: same as the top panel but with extinctions from Yang et al (2012). Note that accretion luminosities have not been measured simultaneously; typical variations can account for a factor as large as ~ 2 (0.3 in logarithmic scale).

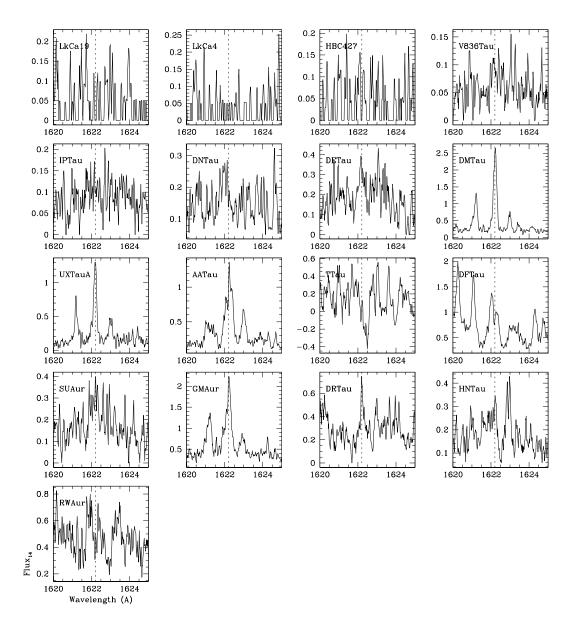


Fig. 13.— P(17)3-9 H_2 profiles of the TTSs in Taurus observed with HST. The rest wavelength is marked for reference. Fluxes are given in units of 10^{-14} erg s⁻¹ cm⁻² Å⁻¹ (F₁₄).

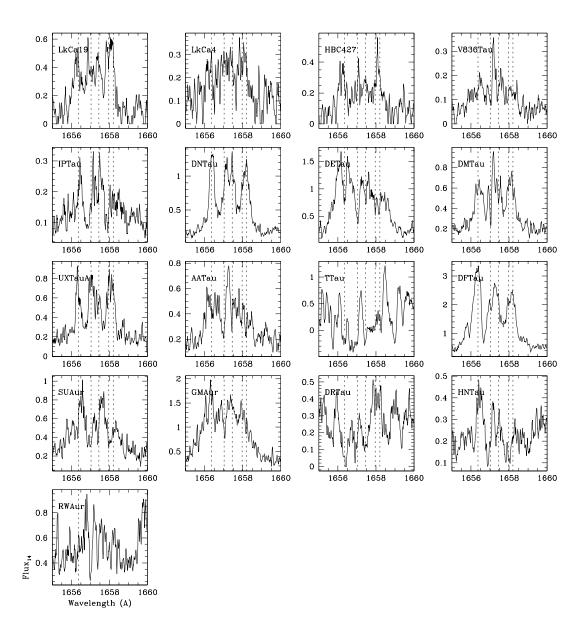


Fig. 14.— C I [uv1] profiles of the TTSs in Taurus observed with HST. The rest wavelength of the lines in the multiplet is marked for reference. Fluxes are given in units of $10^{-14} \text{ erg s}^{-1} \text{ cm}^{-2} \text{ Å}^{-1} \text{ (F}_{14})$.

 $\begin{tabular}{ll} Table & 1: HST/COS observations of the He II line. \\ \end{tabular}$

Star	Instrument/	Observation	Start Time	Exposure	Spec. Initial	Spec. Final
	Grating	ID	(yyyy-mm-dd hh:mm:ss)	Time (sec)	Wavelength (Å)	Wavelength (Å)
SU Aur ³	COS/G160M	LB6B11010	2011-03-25 08:01:38	622.144	1387.748	1748.301
	COS/G160M	LB6B11020	2011-03-25 08:15:08	622.144	1410.706	1771.310
	COS/G160M	LB6B11030	2011-03-25 09:06:57	515.008	1434.646	1795.304
T Tau ¹	STIS/E140M	O5E304020	2000-09-08 09:11:01	2630.173	1140.000	1735.000
	STIS/E140M	O5E304040	2000-09-08 10:56:04	2320.191	1140.000	1735.000
	STIS/E140M	O5E304050	2000-09-08 12:23:56	2630.185	1140.000	1735.000
	STIS/E140M	O5E304060	2000-09-08 14:00:24	2630.164	1140.000	1735.000
LkCa 19 ³	COS/G160M	LB6B28030	2011-03-31 01:21:43	630.112	1387.740	1748.270
	COS/G160M	LB6B28040	2011-03-31 02:33:25	630.112	1410.699	1771.292
	COS/G160M	LB6B28050	2011-03-31 02:47:03	630.112	1434.577	1795.224
$GM Aur^3$	COS/G160M	LB6B01030	2010-08-19 16:53:54	620.192	1387.921	1748.541
	COS/G160M	LB6B01040	2010-08-19 17:07:22	620.192	1410.957	1771.592
	COS/G160M	LB6B01050	2010-08-19 17:20:50	620.192	1431.254	1791.979
RW Aur A^3	COS/G160M	LB6B15010	2011-03-25 02:51:01	539.008	1390.596	1751.126
	COS/G160M	LB6B15020	2011-03-25 03:03:08	538.976	1413.616	1774.208
	COS/G160M	LB6B15030	2011-03-25 03:15:43	538.976	1431.426	1792.083
${\rm HN}~{\rm Tau}^3$	COS/G160M	LB6B09010	2010-02-10 12:49:14	1736.352	1388.187	1755.142
	COS/G160M	LB6B09020	2010-02-10 14:11:51	1396.160	1411.659	1772.251
	COS/G160M	LB6B09030	2010-02-10 15:32:12	1396.160	1435.611	1796.256
UX Tau A^3	COS/G160M	LB6B13030	2010-12-12 14:44:10	647.168	1387.800	1748.355
	COS/G160M	LB6B13040	2010-12-12 14:58:03	647.104	1410.723	1771.317
	COS/G160M	LB6B13050	2010-12-12 15:11:58	647.200	1434.591	1795.276
HBC 427^3	COS/G160M	LB6B26030	2011-03-30 02:34:43	644.992	1387.800	1748.355
	COS/G160M	LB6B26040	2011-03-30 02:48:36	645.120	1410.881	1771.450
	COS/G160M	LB6B26050	2011-03-30 03:02:29	645.088	1434.662	1795.309
$AA Tau^3$	COS/G160M	LB6B07010	2011-01-06 20:30:32	1418.176	1387.834	1748.363
	COS/G160M	LB6B07020	2011-01-06 21:40:00	1387.168	1410.854	1771.435
	COS/G160M	LB6B07030	2011-01-06 22:06:15	1387.136	1434.611	1795.257
$DR Tau^3$	COS/G160M	LB6B14010	2010-02-15 11:08:53	582.016	1388.651	1749.265
	COS/G160M	LB6B14020	2010-02-15 12:04:39	581.952	1411.842	1772.470
	COS/G160M	LB6B14030	2010-02-15 12:17:29	581.984	1435.647	1796.340
LkCa 4^3	COS/G160M	LB6B27030	2011-03-30 07:32:26	600.192	1387.798	1748.330
	COS/G160M	LB6B27040	2011-03-30 07:45:34	600.160	1410.781	1771.352
	COS/G160M	LB6B27050	2011-03-30 07:58:42	600.128	1434.635	1795.284
$V836 \text{ Tau}^3$	COS/G160M	LB6B06010	2011-02-05 05:06:58	1480.192	1393.645	1754.155
	COS/G160M	LB6B06020	2011-02-05 06:12:31	1391.136	1410.840	1771.423
	COS/G160M	LB6B06030	2011-02-05 06:38:50	1391.200	1434.670	1795.307
DE Tau^3	COS/G160M	LB6B08030	2010-08-20 15:14:30	617.152	1387.865	1748.487
22 144	COS/G160M	LB6B08040	2010-08-20 15:27:55	617.184	1410.962	1771.598
	COS/G160M	LB6B08050	2010-08-20 15:41:20	617.088	1434.735	1795.449
IP Tau ³	COS/G160M	LB6B05030	2011-03-21 08:11:35	1179.136	1393.598	1754.105
	COS/G160M	LB6B05010 LB6B05020	2011-03-21 09:15:35	972.192	1407.600	1768.179
	COS/G160M	LB6B05020 LB6B05030	2011-03-21 09:34:45	972.192	1440.509	1801.117
DF Tau^2	COS/G160M	LB3Q020A0	2010-01-11 13:07:29	1324.192	1435.545	1796.229
Dr Tau	COS/G160M	LB3Q020A0	2010-01-11 12:00:02	1408.192	1423.424	1784.071
	COS/G160M	-				
	COS/G160M COS/G160M	LB3Q02080	2010-01-11 11:32:10 2010-01-11 10:24:56	1408.192	1411.793	1772.421
$\mathrm{DM} \; \mathrm{Tau}^3$,	LB3Q02070		1408.192	1400.406	1761.021
DM Tau	COS/G160M	LB6B02030	2010-08-22 17:23:51	978.176	1387.890	1748.500
	COS/G160M	LB6B02040	2010-08-22 18:26:31	1396.128	1410.865	1771.514
DM 70. 3	COS/G160M	LB6B02050	2010-08-22 18:52:45	1396.160	1434.871	1795.561
DN Tau ³	COS/G160M	LB6B04030	2011-09-10 18:14:50	965.120	1435.325	1796.015
	COS/G160M	LB6B04040	2011-09-10 18:34:41	1387.136	1387.879	1748.477
117 m · 4	COS/G160M	LB6B04050	2011-09-10 19:50:39	1387.168	1411.111	1771.74
UZ Tau ⁴	COS/G160M	LBH208020	2011-03-06 22:48:19	1944.288	1384.094	1748.243

Observations obtained under HST proposal 8627 on "Testing the theories of wind/jet production in YSOs" with PI, Nuria Calvet

Observations obtained under HST proposal 11533 on "Accretion flows and winds of PMS stars" with PI, James Green

Observations obtained under HST proposal 11616 on "The disks, accretion and outflows of TTSs" with PI, Gregory Herczeg

⁴ Observations obtained under HST proposal 12161 on "Accretion in close pre-main sequence binaries" with PI, David Ardila

Table 2: COS/G130M observations of the N V line.

Star	Observation	Start Time	Exposure	Spec. Initial	Spec. Final
	ID	(yyyy-mm-dd hh:mm:ss)	Time (sec)	Wavelength (Å)	Wavelength (Å
SU Aur ¹	LB6B11040	2011-03-25 09:19:35	894.048	1132.513	1433.611
	LB6B11050	2011-03-25 09:39:54	894.016	1171.264	1471.991
LkCa 19^1	LB6B28010	2011-03-30 23:21:36	972.032	1132.687	1433.865
	LB6B28020	2011-03-31 00:57:29	972.032	1171.018	1472.086
$GM Aur^1$	LB6B01020	2010-08-19 15:30:01	1064.000	1173.883	1472.056
	LB6B01010	2010-08-19 14:07:11	1064.032	1135.175	1434.068
RW Aur A ¹	LB6B15040	2011-03-25 04:20:18	881.920	1134.524	1433.479
	LB6B15050	2011-03-25 04:40:25	882.016	1171.212	1471.940
$\mathrm{HN}\ \mathrm{Tau}^1$	LB6B09040	2010-02-10 17:01:25	2862.368	1172.119	1472.816
	LB6B09050	2010-02-10 18:37:17	2862.368	1133.578	1434.835
UX Tau A ¹	LB6B13010	2010-12-12 13:21:36	814.016	1132.756	1433.955
	LB6B13020	2010-12-12 13:40:33	813.976	1178.443	1472.069
HBC 427^{1}	LB6B26010	2011-03-29 23:42:24	1116.000	1132.765	1433.914
	LB6B26020	2011-03-30 01:11:12	1007.040	1171.207	1472.055
AA Tau ¹	LB6B07040	2011-01-06 23:15:54	2844.320	1171.275	1471.974
	LB6B07050	2011-01-07 00:51:43	2844.352	1132.673	1433.841
DR Tau ¹	LB6B14040	2010-02-15 12:31:03	851.936	1135.968	1434.705
	LB6B14050	2010-02-15 13:40:31	852.032	1171.490	1467.855
LkCa 4 ¹	LB6B27010	2011-03-30 06:05:02	1152.000	1132.813	1434.013
	LB6B27020	2011-03-30 06:29:21	1152.000	1171.085	1472.155
$V836 \text{ Tau}^1$	LB6B06040	2011-02-05 07:48:28	2852.384	1171.243	1471.854
	LB6B06050	2011-02-05 09:24:21	2852.384	1132.642	1433.753
DE Tau ¹	LB6B08010	2010-08-20 12:23:06	1033.984	1132.918	1431.810
	LB6B08020	2010-08-20 13:50:31	1033.984	1172.592	1472.092
DF Tau ²	LB3Q02030	2010-01-11 07:10:07	1000.192	1136.215	1429.787
	LB3Q02040	2010-01-11 08:20:23	1001.216	1145.843	1439.456
	LB3Q02050	2010-01-11 08:40:31	1410.208	1155.476	1449.112
	LB3Q02060	2010-01-11 09:56:16	1416.192	1165.040	1458.662
IP Tau ¹	LB6B05040	2011-03-21 09:54:41	1439.360	1139.996	1433.623
	LB6B05050	2011-03-21 11:08:05	1852.384	1170.797	1467.013
DM Tau ¹	LB6B02010	2010-08-22 15:19:45	1812.384	1171.278	1472.153
	LB6B02020	2010-08-22 16:50:38	1646.336	1132.819	1434.034
DN Tau ¹	LB6B04010	2011-09-10 15:38:59	1252.320	1171.707	1472.443
	LB6B04020	2011-09-10 16:52:59	1651.360	1133.030	1434.215

 $^{^{1}}$ Observations obtained under HST proposal 11533 on "Accretion flows and winds of PMS stars" with PI, James Green

 $^{^2 \}qquad \text{Observations obtained under HST proposal 11616 on "The disks, accretion and outflows of TTSs" with PI, Gregory Herczeg \\$

Table 3: Main properties of the TTSs

Object	Spectral	L_* (a)	A_V $^{(a)}$	Vsin(i)(.	f) Age (a)	Period	\mathcal{L}_X
	Type	$({\rm L}_{\odot})$	(mag.)	(km/s)	$\log \tau$ (yr)	(d)	$10^{30} {\rm erg \ s^{-1}}$
SU Aur	G1	7.8	0.90	66.2	$6.80 \pm\ 0.08$	3.5	11.641
T Tau	K0	7.8	1.8	20.1		2.8	9.395
LkCa 19	K0	$1.56^{(b)}$	0	19	$7.17 \pm\ 0.01$	2.24	• • •
GM Aur	K3	1.2	1.1	12.4	$6.9 \!\pm 0.2$	12	$0.69^{(d)}$
RW Aur	K4	$1.72^{(b)}$	0.32	17.2	$7.20 \pm\ 0.11$	5.4	
HN Tau	K5	$0.7^{(c)}$	0.52	52.8			$0.18^{(d)}$
UX Tau	K5	$1.29^{(b)}$	0.0	26	$6.43 {\pm} 0.17$		
${\rm HBC}\ 427$	K5Bin	2	0.6				6.3
AA Tau	K7	1.1	1.4	11		8.2	1.039
DR Tau	K7	1.7	1.0	< 10.0	$5.92 \!\pm 0.2$	7.3	
$\rm LkCa~4$	K7	$0.73^{(b)}$	0.69	26.1	$6.43 \pm\ 0.25$	3.38	$1.99^{(d)}$
V836 Tau	K7	$0.8^{\ (d)}$	1.1	< 15.0		6.76	
DE Tau	M0	1.2	1.1	10.0		7.6	$0.025^{(d)}$
IP Tau	M0	0.7	0.9	11.0	$6.6 \!\pm 0.2$	3.3	
DF Tau	M1,M3.5	0.47,0.53 (e	0.04	16.1	$6.28 \pm\ 0.17$	8.5	
DM Tau	M1	0.35	0.6	10	$6.87 \pm\ 0.34$		1.181
DN Tau	M1	1.2	0.8	8.1	$6.15 \pm\ 0.11$	6.6	1.072
UZ Tau	M1	0.31	1.0	15.9			0.736

 $^{^{(}a)}L_*,\, \mathbf{A}_V$ and age as in GdCMA2012 unless otherwise indicated.

 $^{^{(}b)}$ Bertout et al. 2007.

 $^{^{(}c)}L_{\ast}$ in Table 1 from Ingleby et al. 2009 too small. Kenyon & Hartmann 1995 used instead.

 $^{^{(}d)}$ Hao Yang et al. 2012

⁽e) uminosities of DF Tau A and DF Tau B are provided (from Bertout et al. 2007).

 $^{^{(}f)}$ Clarke & Bouvier 2000

Table 4: Measurements and data

Object	F(He II)	F ₁₆₆₆ (O III]) ^{(a}	F (N V) ^(b)	F ₁₃₃₈ (H ₂)	F _{1489.636} (H ₂)
$(10^{-14} \text{ erg s}^{-1} \text{ cm}^{-2})$					
SU Aur	$2.05 \pm\ 0.13$	$0.46 \pm~0.18~^w$	$0.53 \pm~0.05~^c$	2.82 ± 0.14	0.41 ± 0.04
T Tau	$4.87 \pm\ 0.96$	$1.14\pm~0.41$ w			• • •
LkCa 19	$1.43 \pm\ 0.10$		$0.22 \pm~0.03~^n$		
GM Aur	$6.22 \pm\ 0.19$		$2.17\pm~0.22$ n	8.76 ± 0.67	1.08 ± 0.06
RW Aur	$0.66 \pm\ 0.12$	$2.10\pm~0.43$ s	0.66 \pm 0.11 b	6.49 ± 0.91	3.26 ± 0.15
HN Tau	$1.33 \pm\ 0.26$	1.24 ± 0.26 i	$0.27 \pm~0.03$ c	4.45 ± 0.23	1.04 ± 0.07
UX Tau	$2.25 \pm\ 0.12$		$0.88\pm~0.08$ c	4.29 ± 0.21	0.85 ± 0.03
${\rm HBC}\ 427$	$0.77 \pm\ 0.10$		$0.08\pm~0.02$ n		
AA Tau	$2.93 \pm\ 0.06$		0.14 ± 0.01^c	9.12 ± 0.24	1.16 ± 0.05
DR Tau	$0.93 \pm\ 0.15$	2.14 ± 0.49 s	0.25 ± 0.05^c	2.33 ± 0.34	0.52 ± 0.09
$\rm LkCa~4$	$0.54 \!\pm 0.06$		0.07 ± 0.01^n		
V836 Tau	$0.44 \pm\ 0.03$		0.07 ± 0.01^{c}	0.45 ± 0.05	0.15 ± 0.01
DE Tau	$0.87 \!\pm 0.16$	0.27 \pm 0.11 i	0.35 ± 0.05^b	2.76 ± 0.28	0.45 ± 0.05
IP Tau	1.33 ± 0.04		0.08 ± 0.02^c	0.17 ± 0.05	0.13 ± 0.02
DF Tau	$7.32 \pm\ 0.20$	1.42 ± 0.47 s	1.07 ± 0.07^{b}	$15.9 \!\pm 0.6$	0.94 ± 0.07
DM Tau	$7.28 \pm\ 0.18$		0.68 ± 0.10^c	6.72 ± 0.31	0.61 ± 0.03
DN Tau	6.53 ± 0.06		0.88 ± 0.08^n	0.88 ± 0.13	0.15 ± 0.04
UZ $Tau^{(c)}$	$1.06 \pm\ 0.34$	0.43 ± 0.33			0.55 ± 0.02

 $^{^{(}a)}w,i$ and s stand for weak, intermediate and strong line, respectively. The flux in the 1660.802 Å line has only been measured for strong sources. F_{1660} is equal to $(0.37\pm0.32)\times10^{-14}$ erg s⁻¹ cm⁻² for DF Tau, $(0.34\pm0.23)\times10^{-14}$ erg s⁻¹ cm⁻² for DR Tau and $(0.46\pm0.23)\times10^{-14}$ erg s⁻¹ cm⁻² for RW Aur.

^(b)The line flux may be affected by the H₂ feature. A quality flag has been inserted. Fluxes flagged with ^b (strong blends), ^c (clean blends where the H₂ and N V contributions can be separated) and ⁿ (no H₂ emission is detected).

^(c)UZ Tau is a close binary and observations during various phases are available. H₂ lines flux is constant but He II and O III] fluxes are variable. The values provided in the table correspond to the mean and standard deviation of the measured fluxes during the cycle. During the cycle the He II and O III] fluxes vary by a factor of 3.

Table 5: UV lines profiles dispersion

		0	0	
Stars	$\sigma(\mathrm{H_2\ 1339\AA})$	$\sigma(\mathrm{H}_2\ 1489\mathrm{\AA})$	$\sigma(N~V~1238~\text{Å})$	$\sigma(\text{He II})$
	$({\rm km~s^{-1}})$	$({\rm km~s^{-1}})$	$({\rm km~s^{-1}})$	$({\rm km~s^{-1}})$
AATau	52.38	33.32	89.66	40.19
DETau	39.61	26.72	79.97	68.05
DFTau	52.38	36.71	116.3	48.66
DMTau	48.51	21.8	138.1	88.85
DNTau	48.51	39.81	36.35	39.7
DRTau	34.3	34.49	70.27	70.34
GMAur	65.69	30.85	123.6	62.25
HNTau	56.01	29.54	130.9	87.04
IPTau	19.81	33.32	72.7	32.58
SUAur	28.01	26.72	143	63.9
UXTau	34.3	23.55	99.35	58.41
V836Tau	34.3	32.1	67.85	33.26
LkCa19			33.93	41.47
LkCa4			38.77	36.05

Star	T_1	T_2	EM_1	EM_2	$\mathrm{EM}_1/\mathrm{EM}_2$
	(MK)	(MK)	10^{52}	10^{52}	
T Tau	4.52	23.65	33.86	57.85	0.585
SU Aur	5.22	23.30	87.01	32.45	2.681
HBC 427	9.04	28.06	14.98	15.07	0.994

Table 7: Shift of the He II narrow emission component

Stars	$\Delta \lambda = \lambda_{peak} - \lambda_0$		
	(Å)		
AATau	.175		
DETau	.202		
DFTau	.188		
DMTau	.166		
DNTau	.164		
DRTau	.115		
GMAur	.186		
IPTau	.151		
UXTau	.13		
V836Tau	.166		